Neutron and X-ray Scattering Studies of Structural Phase Transitions and Soft Modes in Rb_2ZnBr_4

H Shigematsu† ‡, H Mashiyama§, Y Oohara‖ and K Ohshima†

† Institute of Applied Physics, University of Tsukuba, Tsukuba 305-3573, Japan

§ Department of Physics, Faculty of Science, Yamaguchi University, Yamaguchi 753-8512, Japan

‖ Institute for Solid State Physics, University of Tokyo, Roppongi, Tokyo 106-8666, Japan

Abstract. The low-temperature phase transitions of rubidium tetrabromozincate have been investigated with the use of neutron and X-ray scattering techniques to clarify the mechanism of the transitions and to determine the space groups of the low-temperature phases. The low-frequency excitations which soften at the phase transition $T_3 = 112$ K have been measured by the inelastic neutron scattering technique. On the other hand, no soft phonon mode which makes a contribution to the phase IV-to-V transition at $T_4 = 76$ K has been observed. Both in phases IV and V, superlattice reflections appear at the position $\frac{h}{2}\frac{k}{2}\frac{l}{3}$, where the Miller indices h, k and l are referred to the lattice constants of phase I. In phase V, new Bragg reflections emerge at the position $hk0$: $h + k = 2n + 1$ and increase continuously with decreasing temperature. The space groups are considered to be $P11b$ with $Z = 24$ for phase IV and $C1c1$ with $Z = 48$ for phase V according to general group theoretical considerations. Furthermore, structural models for phase IV are proposed to explain the extra extinction rule, the antiferroelectricity and other observed character of the crystal.

PACS numbers: 64.70.-p, 63.20.-e, 77.80.Bh, 61.12.-q

1. Introduction

Rubidium tetrabromozincate, Rb_2ZnBr_4, belongs to a family of A_2BX_4-type ferroelectrics with the β-K_2SO_4 type structure as similar as Rb_2ZnCl_4 [1]. The normal phase (phase I) has an orthorhombic structure (space group: $Pmcn$, $Z = 4$), where the c-axis is a pseudo-hexagonal axis, and $b \simeq \sqrt{3}a$. As temperature decreases the crystal transforms into an incommensurate phase (phase II) at $T_{\rm i} = 347\,{\rm K}$ [2, 3]. In

‡ Present address: Department of Quantum Engineering, Graduate School of Engineering, Nagoya University, Nagoya 464-8603, Japan.

phase II, the modulation wave vector is given by $q = (\frac{1}{3} - \delta)c_0^* \simeq \frac{5}{17}c_0^*$, where δ and c_0^* stand for the misfit parameter and the reciprocal-lattice parameter in the normal phase, respectively. The wave vector is almost independent of temperature except in the close vicinity of the lock-in transition point ($T_C = 187\,K$) [4, 5], below which the structure is commensurate with the wave vector of $q = \frac{c_0^*}{3}$. Phase III shows a ferroelectric property along the a-direction (space group: $P2_1cn$, $Z = 12$) and the ferroelectricity remains down to 4 K [1, 6].

Many of the A_2BX_4-type ferroelectrics, for example, Rb_2ZnCl_4, K_2ZnCl_4 and K_2CoCl_4, undergo the same successive phase transition; phase I, phase II and phase III. At lower temperature, a further phase transition takes place at 74 K (Rb_2ZnCl_4), 145 K(K_2ZnCl_4) and 142 K(K_2CoCl_4) [7]. In the lowest temperature phase the superlattice reflections were observed at $\frac{h}{2}\frac{k}{2}\frac{l}{3}_{Pmcn}$, where the indices are referred to the unit cell of phase I, which is indicated by subscript $Pmcn$. The superlattice phase is reported to have a space group $C1c1$ [8].

On the other hand, in Rb_2ZnBr_4 two phase transitions have been reported at $T_3 = 112\,K$ and $T_4 = 76\,K$, and slight dielectric anomalies were also observed at 56 and 10 K [6]. A soft Raman mode has been observed for the scattering orientation $b(cc)a$ below T_3 [9], and the type of the phase transition at T_3 is considered to be a displacive one. In phase IV between T_3 and T_4, antiferroelectricity along the b-direction is reported and the superlattice reflections were observed at the $\frac{h}{2}\frac{k}{2}\frac{l}{3}_{Pmcn}$ below T_3 in similar to other A_2BX_4-type ferroelectrics [10]. In phase V below T_4, the ferroelectricity appears both along the a- and the c-directions [6]. The existence of monoclinic domains has been confirmed by optical activity [11].

Furthermore, the appearance of Bragg reflections at the position $hk0_{Pmcn}$: $h + k = 2n + 1$ has been reported in phase V [12]. But the difference of reflection conditions between phases IV and V have not been recognized [10]. That is, the structural features of phase IV and V are not clearly characterized as yet. Several authors have predicted the space groups of low-temperature phases; $C1c1$ in phase IV, and $C1c1$ or $P1$ in phase V. However, the crystal structures have not been determined [10, 12, 13, 14].

As for the phase IV, three possible space groups were proposed; monoclinic forms ($C1c1$ and $P11b$) and a triclinic one ($P1$) [15]. On the contrary, it has been reported that the crystal symmetry of phase IV is orthorhombic from the observation of the crystal habit [11, 16].

In order to clarify the mechanism of the transitions at T_3 and T_4 and the structures in low temperature, we have performed both neutron and X-ray scattering experiments. In section 2, experimental procedures of the scattering studies are described in detail. The results of inelastic neutron and elastic X-ray scattering studies below room temperature are presented in section 3. Phase transitions and structures in low temperature are discussed in the final section.

2. Experimental

Single crystals of Rb_2ZnBr_4 were grown by a slow evaporation method from an aqueous solution at 308 K. Although the molar ratio of AX versus BX_2 in the aqueous solution is usually 2 : 1 in the A_2BX_4-type ferroelectrics, there are some exceptions; *e.g.* $(NH_4)_2ZnCl_4$ [17], and $(NH_4)_2ZnBr_4$ [18], in which the ratio 1 : 1 rather than 2 : 1 is appropriate to get single crystals. In Rb_2ZnBr_4, we made sure that single crystals were grown from the ratio between 2 : 1 and 1 : 1. Furthermore, since experience had shown that high-quality and large single crystals could more easily be grown from the ratio 1 : 1 than the ratio 2 : 1, we used the aqueous solution of the ratio 1 : 1 in Rb_2ZnBr_4. It took about three months to obtain large single crystals. The crystals were transparent and showed cleavage for a plane perpendicular to the b-axis. The samples were annealed at 393 K in air for ten hours before an experiment, to avoid the influence of included water [21].

The triple-axis spectrometer C1-1 installed in the guide hall at JRR-3M research reactor of Japan Atomic Energy Research Institute (JAERI), Tokai, was used for neutron scattering. A crystal with a volume of 6.9 cm^3 was mounted in an aluminum can which was set in a closed-cycle He-refrigerator (CTI). The sample temperature was controlled within 0.1 K by a TEMCON-IV system developed by Y. Noda of Chiba University, Japan. Energy scans to observe phonon spectra were done with a fixed incident neutron wave number $k_i = 1.55$ Å^{-1} with a pyrolytic graphite monochromator and an analyzer. A beryllium filter was used in order to cut off higher-order reflections and a beam collimation of open-open-80'-80' was employed. The full width at half maximum (FWHM) of a Bragg peak by ω-scan method was 0.4°. A typical instrumental energy resolution was 0.2 meV (FWHM) for a constant-Q scan.

In the inelastic scattering experiments, the data were collected in the (a^*, b^*) scattering plane. Phonon dispersion curves were measured along the lines $(2+\xi\ 2-\xi\ 0)_{Pmcn}$: $\xi < 0.5$ and $(1-\xi\ 4+\xi\ 0)_{Pmcn}$: $\xi \geq 0.5$. On the former line, the reflection 220_{Pmcn} was strong and an acoustic branch was observed. On the latter line, acoustic branch was not observed because the 050_{Pmcn} reflection is absent by an extinction rule of phase III [19, 20]. For both lines, transverse components were mainly detected because phonon propagation vector was nearly perpendicular to scattering vector. It should be noted that the reflections $\frac{5}{2}\frac{3}{2}0_{Pmcn}$ and $\frac{1}{2}\frac{9}{2}0_{Pmcn}$ were strong superlattice reflections below T_3. Lattice parameters were determined as $a = 7.63$ Å and $b = 13.30$ Å at 250 K from the peak positions of 200_{Pmcn} and 040_{Pmcn}.

The X-ray diffraction measurements were performed by using a four-circle diffractmeter (Huber $422 + 511.1$) attached to a rotating-anode-type generator (Rigaku RU-300) with an X-ray power of 50 kV×150 mA. Two different settings were used. First, for the measurements of angles α, β and γ, and the examination of whether an

incommensurate phase exists or not in phase IV, the incident beam (Mo-Kα_1 radiation) from a Mo target was monochromated by Ge111 with getting a good resolution. Mo-Kα_2 radiation was cut off by the knife edges of a divergent slit with 0.2 mm in width and 0.2 mm in height. The FWHM of a Bragg reflection was less than 0.04° under the setting.

Second, for the investigation of extinction rules and the measurements of peak intensities, the incident beam (Mo-Kα) was monochromated by pyrolytic graphite (HOPG) to increase the reflection intensity. A collimator of 0.8 mm in diameter was used to pass the incident beam.

Furthermore we have used an imaging-plate system installed at Photon Factory (PF) of National Laboratory for High Energy Physics, Tsukuba, in order to observe a wide region of reciprocal-lattice space.

Single-crystal specimens used in the experiment were cut into a size of 1, 2 and 3 mm along *a*-, *b*- and *c*-axes, respectively, or an almost spherical shape with a diameter of 0.25 mm. The sample was mounted on a copper sample holder, which was fixed on the cold head of a closed-cycle cryogenic refrigerator (Air Products, DE201), with the *a*- or *b*- or *c*-axis as a rotation axis. The temperature of the sample was controlled within 0.1 K by the TEMCON-IV system.

3. Results

3.1. Neutron scattering

Figures 1 and 2 show the phonon dispersion curves in an extended-zone scheme along the (ξ ξ 0) line and a typical energy scan with constant Q within the optic mode region at 130 K, respectively. The observed phonon peaks were fitted to a double Lorentzian-type cross-section convoluted with an instrumental resolution function. Two modes, which were anticrossed to each other around $\xi \sim 0.7$, were observed. One is a transverse optic (TO) mode degenerated with a transverse acoustic (TA) branch at the zone boundary S point ($\frac{1}{2}\frac{9}{2}0_{Pmcn}$, *i.e.* $\xi = 0.5$). Another is a TO branch whose frequency is higher than the degenerated TO mode at the same ξ position. In figure 1, the solid curve for the degenerated TO mode is obtained with least-squares fitting to a Fourier decomposition;

$$E(\xi)^2 = \sum_{n=1}^{5} F_n \left[1 - \cos(n\pi\xi)\right], \tag{1}$$

like the dispersion relation of Λ_2 and Λ_3 branches in the extended scheme of K_2SeO_4 [22]. The coefficients F_n correspond to the generalized effective interlayer force constants for coupling layers in the crystal separated by a distance of $\frac{nb}{2}$. The values of F_n from $n = 1$ to 5 are determined as 0.98(6), −0.52(4), 0.25(5), 0.70(4) and −0.10(4) meV^2 at 130 K. On the other hand, the solid line for the higher TO branch is just a guide to the

eye. Figure 3 shows the phonon dispersion curves of the degenerated TO mode at four temperatures above T_3. Solid lines are fitted with the use of equation (1). The values of F_n from $n = 1$ to 5 obtained are 1.29(7), −0.47(5), 0.25(5), 0.82(5) and −0.22(5) meV^2 at 160 K, 1.90(7), −0.29(5), 0.42(6), 0.76(5) and −0.30(5) meV^2 at 250 K and 2.48(5), −0.25(4), 0.57(5), 0.53(5) and −0.29(5) meV^2 at 290 K. The force constant between nearest-neighbor layers, F_1, decreases sharply with decreasing temperature. The force constant F_4 is larger than F_2 and F_3 with the exception of value at 290 K and increases slightly with decreasing temperature. It is clear that this mode softens in the vicinity of the S point with decreasing temperature.

The temperature dependence of energy scans with constant Q below T_4 at the S point and at $\xi = 0.55$ is shown in figure 4 and figure 5. Two temperature-dependent modes are clearly observed. The higher-energy mode (soft mode S) is identified as the soft mode reported by Francke *et al*. [9]. The lower-energy mode (soft mode A) is a new one observed for the first time in this neutron-scattering study.

The peak intensity of the soft mode S is weaker than that of the soft mode A around the S point. By using the higher resolution setting with the beam collimation of open-open-40'-40' we have ascertained that the soft mode A remains around T_4 where the mode does not soften and therefore does not contribute to the phase IV-to-V transition. The dispersion relation at 50 K is shown in figure 6 as an example in low-temperature phase V. In the vicinity of $\xi = 0.5$ and 1, TA branches are observed clearly because the S point ($\xi = 0.5$) becomes equivalent to a Γ point and the reflections $\frac{1}{2}\frac{9}{2}0_{Pmcn}$ and 050_{Pmcn} become Bragg reflections below T_3 and T_4, respectively. In the figure, the solid line of the soft mode A is obtained by a fitting to equation (1). The other two lines for the degenerated TO and higher TO modes are drawn as a guide to the eye. Although it may be reasonable to expect that the TA mode interacts with the mode A, the TA branch becomes so broad and weak away from $\xi = 0.5$ or 1 that it was difficult to confirm the anticrossing. In figure 6, the clearly observed peak was regarded as mode A.

Figure 7 shows the temperature dependence of the observed mode frequencies at the S point, in which the solid curves are fitted according to the following relations:

$$E = C(T - T_3)^{0.5};$$
the degenerated TO mode above T_3, (2)

$$E = C(T_3 - T)^{0.5};$$
the soft mode S below T_3, (3)

$$E = C(T_3 - T)^{B}; \quad \text{the soft mode A below } T_3. \tag{4}$$

The values of C are obtained as 0.099, 0.181 and 0.015 meV K$^{-\frac{1}{2}}$ for equations (2) to (4). In equation (4), B is used as a fitting parameter instead of 0.5 and the value obtained by the least-squares fitting was 0.84. It is clear that the degenerated TO mode and soft

modes S and A make a contribution to the phase III-to-IV transition.

On the other hand, the higher TO mode shows a weak softening as the temperature approaches T_3 from above, and does not vanish, but hardens with further decreasing temperature. Below 100 K, it was difficult to determine the peak position accurately, because the intensity became so weak with decreasing temperature.

3.2. X-ray scattering

Figure 8 shows the ω-scan profiles of the 400_{Pmcn} reflection with the b-axis as the rotating axis below T_3. A splitting of the Bragg reflection took place below T_4 and the separation increased continuously with decreasing temperature. Since the $0k0_{Pmcn}$ nor $00l_{Pmcn}$ Bragg reflections did not split, the splitting of the $h00_{Pmcn}$ type Bragg reflections exhibits the existence of a monoclinic twin in phase V. The temperature dependence of the deviation angle $\Delta\beta = \beta - 90^\circ$ on cooling is plotted in figure 9; $\Delta\beta$ is 0.055° at 20 K. The other angles, α and γ, were 90° within the experimental error in phases IV and V. Note that the peak splitting of superlattice reflections $\frac{h}{2}\frac{k}{2}\frac{l}{3}_{Pmcn}$, which has been reported in K_2ZnCl_4 [23], was not observed in phase IV. Therefore the structure is a commensurate one.

In addition to the appearance of superlattice reflections below T_3, the Bragg reflections at the position $hk0_{Pmcn}$: $h + k = 2n + 1$ appeared at T_4 and increased in intensity with increasing temperature [24]. The temperature dependence of integrated intensities of the 410_{Pmcn} reflection on heating and on cooling is shown in figure 10. We could not recognize any thermal hysteresis between heating and cooling processes. The temperature dependence of the integrated intensity I can be fitted to the following function;

$$I = A(T_4 - T)^{2\beta}, \tag{5}$$

where A and T_4 denote the proportional coefficient and the phase transition temperature, respectively. The values of T_4 and β are 75.84(8) K and 0.283(3) on heating, and 75.95(13) K and 0.281(4) on cooling, respectively.

Just above T_4, the peak intensity seemed to remain weak, but the width became a little broader; although it was not so broad as the diffuse scattering which can be observed at the phase III-to-IV transition at the superlattice reflection positions. We consider that the residual intensity in phase IV is caused by a local strain from the twined structure of phase IV, and that the reflections with $hk0_{Pmcn}$: $h + k = 2n + 1$ are absent systematically in phase IV. The change of the extinction rules between phases IV and V was observed in this way. Both our results and those of others [6, 10, 12] are tabulated in table 1, where the Miller indices h_s, k_s and l_s are referred to the $a_0 \times b_0 \times 3c_0$ superlattice cell of phase III and to the $2a_0 \times 2b_0 \times 3c_0$ one of phases IV and V. That is to say, the 410_{Pmcn} reflection in figure 10 corresponds to the 820_{phaseV} reflection in

phase V.

As a result of using the imaging-plate system installed at PF, no other extra reflection was observed at any temperature. Furthermore in phases III, IV and V, the observed structure factors $|F(\pm h_{\rm s} \ \pm k_{\rm s} \ \pm l_{\rm s})|$ assumed almost equal magnitudes within experimental errors. The observed diffraction patterns had symmetry D_{2h} of the orthorhombic system.

4. Discussion

4.1. Behavior of zone-boundary soft modes

By inelastic neutron scattering experiments for the low-temperature phase transitions at $T_3 = 112$ K and $T_4 = 76$ K, we have shown that the dispersion relations depend strongly on temperature and the four low-energy phonon modes exist below room temperature. Three of them, the degenerated TO mode ($T > T_3$) and the soft modes S and A ($T < T_3$), are confirmed to make a contribution to the phase transition at T_3, because the frequencies of these modes tend to zero upon approaching T_3. On the other hand, the higher TO mode has no direct connection with III-to-IV nor IV-to-V transition, and the frequency remains finite at the transition temperatures. Furthermore, a behavior of anticrossing of the degenerated TO mode with the higher TO mode is clearly observed from room temperature down to T_3. As a consequence of the temperature-dependence of the force constants with the phonon dispersion curve of the degenerated TO mode, the softening results from the decrease of F_1, F_2 and F_3 in the presence of a strong and persisting force with a range $2b$ with magnitude F_4.

From group theoretical considerations, Dvorak and Kind [15] showed that three space groups, $P11b$, $C1c1$ and $P1$ are possible if the degenerated zone-boundary mode freezes in the A_2BX_4-type crystals. According to the theory, the mode splits into the totally symmetric mode S and the antisymmetric mode A. In Rb_2ZnBr_4, it is natural to consider that the higher-energy and the lower-energy modes are worthy of mode S and A, respectively, because the soft mode S corresponds to the $b(cc)a$ Raman mode below T_3 [9]. It should be noted that in Rb_2ZnCl_4 the soft mode A has not been observed yet [8, 25]. The excitation energy of the soft mode A is so low that it could not be recognized under the used energy resolution. Although no hysteresis was observed in the integrated intensity around T_4 as shown in figure 10, this transition should be of first order because the transition is accompanied by a latent heat release in the measurement of heat capacity [26] and the spontaneous polarization along the c-axis changes discontinuously [6]. Furthermore, the integrated intensity has a steep temperature dependence as if the exponent obtained is 0.283(3) on heating or 0.281(4) on cooling. These values are smaller than the classical exponent $\beta = 0.5$ and $\beta = 0.35$ determined experimentally in previous works [8, 10]. Such a small exponent may suggest that the transition is of first

order.

4.2. Structure of low-temperature phases

As shown in table 1, we recognized differences in reflection conditions between phases IV and V, which are schematically demonstrated in figure 11. Large full circles, small full circles and open circles, and open triangles indicate existing positions of the Bragg reflections in phase III, the additional superlattice ones in phase IV and the additional Bragg ones in phase V, respectively. $A^*_{\rm IV}$, $B^*_{\rm IV}$, $A^*_{\rm V}$ and $B^*_{\rm V}$ stand for the reciprocal vectors.

In phase IV, the following extinction rule for systematic absence was confirmed;

$$h_{\rm s}k_{\rm s}0:\ h_{\rm s}+k_{\rm s}=4n+2 \text{ and } h_{\rm s},\ k_{\rm s}=2n \tag{6}$$

under the $2a_0 \times 2b_0 \times 3c_0$ supperlattice unit cell. Taking our results and other ones, for instance, dielectric measurements [1, 6] and space-group analysis [15] into account, we assign the twin structure of space group $P11b$ with $Z = 24$ (referred to as model $\rm IV_A$ hereafter). This monoclinic structure is formed by unit cell vectors related with that of the normal phase as

$$\boldsymbol{A}_{\rm IV}=\boldsymbol{a}_0-\boldsymbol{b}_0,\ \boldsymbol{B}_{\rm IV}=\boldsymbol{a}_0+\boldsymbol{b}_0 \text{ and } \boldsymbol{C}_{\rm IV}=3\boldsymbol{c}_0. \tag{7}$$

The proper symmetry operations of this phase are

$$\begin{aligned}&[1]_{\rm A}\quad x,\ y,\ z \quad\text{and}\\ &[2]_{\rm A}\quad x,\ y+\frac{1}{2},\ \overline{z}+\frac{1}{2}.\end{aligned} \tag{8}$$

Here the operation $[2]_{\rm A}$ corresponds to one of the n-glide of $P2_1cn$ of phase III. Reflections $h_{\rm s}k_{\rm s}0:\ h_{\rm s}+k_{\rm s}=4n+2$ or $h_{\rm s}+k_{\rm s}=2n+1$ are absent in only single domain model. If the structure of phase IV is considered as the twin structure with the domain ratio of 1 : 1, then the obtained extinction rules (except for $h_{\rm s}0l_{\rm s}$: $l_{\rm s}=2n+1$) as well as the existence of antiferroelectricity along the b-axis can be explained straightforwardly. In figure 11, large full circles and small full circles indicate positions of the reflections for the single domain structure characterized by the operations $[2]_{\rm A}$ and $[2]_{\rm B}$. Moreover, small open circles indicate positions of the reflections for another twined structure. Note that overlapping the reflections (large full circles) for the twined structure with those for the single domain structure. In this twin model, there is no inevitable reason that the crystal system is orthorhombic. The three angles have values of 90° under the $2a_0 \times 2b_0 \times 3c_0$ unit cell, accidentally.

In phase V, the formation of twin structure also occurs. In accordance to the crystal system (monoclinic) and the extinction rule, the space group should be $C1c1$

with $Z = 48$, which permits the spontaneous polarization within the a-c plane. This monoclinic structure is formed by the following superlattice cell vectors

$$\boldsymbol{A}_{\rm V} = 2\boldsymbol{a}_0,\ \boldsymbol{B}_{\rm V} = 2\boldsymbol{b}_0 \text{ and } \boldsymbol{C}_{\rm V} = 3\boldsymbol{c}_0. \tag{9}$$

A primitive cell of phase V can be defined by the unit cell of phase IV. Figure 12 shows the schematic picture of the structure projected along the c-axis between $z = 0$ and $\frac{1}{3}$ in phases III, IV or V [27]. In the figure, $ZnBr_4$ tetrahedra are indicated by triangles and are set at the mean positions of the normal structure. All Rb ions are omitted for simplicity. The origin of phase V is translated to $\boldsymbol{b}_0/4$ from phase IV [27]. The primitive unit cells in phases III, IV (model $\rm IV_A$) and V are denoted by dotted, dashed and solid lines, respectively.

Now we present other models for phase IV, which inevitably must satisfy all the extinction rules given in table 1 and the orthorhombic system as well as the existence of antiferroelectricity along the b-axis. We consider additional symmetry operations on the basis of the groupoids [28, 29]. These structure (referred to as models $\rm IV_B$, $\rm IV_C$ and $\rm IV_D$ hereafter) are formed by the same unit cell defined by relation (7) for models $\rm IV_B$ and $\rm IV_C$ and relation (9) for model $\rm IV_D$. The symmetry operations are given in table 2. The characteristics of phase IV can be explained by the partial remnant of these additional symmetries, $[3]_{\rm B}$ and $[4]_{\rm B}$ for model $\rm IV_B$, $[3]_{\rm C}$ and $[4]_{\rm C}$ for model $\rm IV_C$ and from $[5]_{\rm D}$ to $[8]_{\rm D}$ for model $\rm IV_D$, which correspond to the symmetries of phase III. The structure of models $\rm IV_B$ and $\rm IV_C$ is based on the structure with space group $P11b$ of phase IV. The symmetry operations should contain the operations $[3]_{\rm B}$ and $[4]_{\rm B}$ or $[3]_{\rm C}$ and $[4]_{\rm C}$ in addition to the proper ones of (8). Pairs of operations $[1]_{\rm A}$ and $[3]_{\rm B}$, $[2]_{\rm A}$ and $[4]_{\rm B}$, $[1]_{\rm A}$ and $[3]_{\rm C}$ and $[1]_{\rm A}$ and $[4]_{\rm C}$ correspond to the c-glide operations of phase III. Then the crystal system becomes orthorhombic C_{2v}. The difference between the model $\rm IV_A$ and models $\rm IV_B$ and $\rm IV_C$ is whether the extinction rule $h_{\rm s}0l_{\rm s}$: $l_{\rm s} = 2n + 1$ holds approximately (accidentally) or exactly (inevitably). On the other hand, the structure of model $\rm IV_D$ is based on the structure with space group $C1c1$ of phase V. The set of operations from $[1]_{\rm D}$ to $[4]_{\rm D}$ and from $[5]_{\rm D}$ to $[8]_{\rm D}$ are corresponding to those of the $C1c1$ structure. The relation between $[1]_{\rm D}$ and $[5]_{\rm D}$ is not a group element, however, it leads to the extra extinction rule of equation (6). The point group of the model $\rm IV_D$ is a orthorhombic C_{2v}, which satisfies the X-ray scattering result and the dielectric nature of phase IV.

The full reflection conditions and the relation of magnitude with eight structure factors $|F(\pm h_{\rm s}\ \pm k_{\rm s}\ \pm l_{\rm s})|$ of phase IV are satisfied by considering the same twin structure as the structure of model $\rm IV_A$, $\rm IV_B$, $\rm IV_C$ or $\rm IV_D$. If the domain ratio of the monoclinic twin is 1 : 1 in phases IV and V, then all eight structure factors $|F(\pm h_{\rm s}\ \pm k_{\rm s}\ \pm l_{\rm s})|$ have the same magnitude and the observed symmetry D_{2h} of phase IV can be explained directly. When the domain ratio deviates from 1 : 1, the relationship of these structure

factors changes as shown in table 3. Therefore, when the domain ratio is not equal to $1:1$, the structure of phase IV can be decided either model $\mathrm{IV_A}$, $\mathrm{IV_B}$, $\mathrm{IV_C}$ or $\mathrm{IV_D}$. In both models $\mathrm{IV_B}$ and $\mathrm{IV_C}$, the relationship of these structure factors is the same and the agreement between the observed and calculated structure factors for many reflections is required in order to determine which model is realized. However, according to the results of X-ray scattering, the domain ratio is almost $1:1$ within the experimental errors and we could not definitely determine it. Incidentally, it has been reported that the domain ratio of the $C1c1$ structure in $\mathrm{K_2CoCl_4}$ was $1.014:0.986$ [27].

As noted in section 4.1, the IV-to-V transition is a first-order one. Usually the space groups changes at the transition. If this is also the case, the space group of phase IV is $P11b$, since that of phase V is $C1c1$ definitely. The model $\mathrm{IV_B}$ or $\mathrm{IV_C}$ is plausible to explain the orthorhombic crystal system. In order to make clear which model really represents the phase IV, it is desirable to collect scattering intensities very carefully and refine the crystal structure very accurately.

Acknowledgments

One of the authors (H.S.) would like to thank Dr. A. Yamamoto of National Institute for Research in Inorganic Materials for helpful discussions, and to Prof. Y. Noda of Chiba University for fruitful discussions and technical support in neutron and X-ray scattering experiments.

Reference

[1] Sawada S, Shiroishi Y, Yamamoto A, Takashige M and Matsuo M 1977 *J. Phys. Soc. Japan* **43** 2101

[2] De Pater C J and Van Dijk C 1978 *Phys. Rev.* **B18** 1281

[3] De Pater C J, Axe J D and Currat R 1979 *Phys. Rev.* **B19** 4684

[4] Gesi K and Iizumi M 1978 *J. Phys. Soc. Japan* **45** 1777

[5] Iizumi M and Gesi K 1983 *J. Phys. Soc. Japan* **52** 2526

[6] Yamaguchi T and Sawada S 1991 *J. Phys. Soc. Japan* **60** 3162

[7] Cummins H Z 1990 *Phys. Rep.* **185** 211

[8] Mashiyama H, Sugimoto K, Oohara Y and Yoshizawa H 1992 *J. Phys. Soc. Japan* **61** 3042

[9] Francke E, Le Postollec M, Mathieu J P and Poulet H 1980 *Solid State Commun.* **35** 183

[10] Kasano H, Shigematsu H, Mashiyama H, Iwata Y, Kasatani H and Terauchi H 1994 *J. Phys. Soc. Japan* **63** 1681

[11] Meekes H and Janner A 1988 *Phys. Rev.* **B38** 8075

[12] Ueda T Iida S and Terauchi H *J. Phys. Soc. Japan* 1982 **51** 3953

[13] Hogervorst A C R and Helmholdt R B 1988 *Acta Crystallogr.* **B44** 120

[14] Belobrova I A, Aleksandrova I P and Moskalev A K 1981 *Phys. Status Solidi* (a) **66**, K17

[15] Dvorak V and Kind R 1981 *Phys. Status Solidi* (b) **107** K109

[16] Hogervorst A C R and Helmholdt R B 1988 *Acta Crystallogr.* **B44** 120

[17] Meerburg P A 1903 *Z. Anorg. Chem.* **37** 199

[18] Shigematsu H, Kasano H and Mashiyama H 1993 *J. Phys. Soc. Japan* **62** 3929

[19] Quilichini M, Dvorak V and Boutrouille 1991 *J. Phys. I France* **1** 1321

[20] Mashiyama H, Sugimoto K, Oohara Y and Yoshizawa H 1992 *J. Phys. Soc. Japan* **61** 3042

[21] Takai S, Akake T and Gesi K 1993 *J. Phys. Chem. Solids* **54** 213

[22] Iizumi M, Axe J D, Shirane G and Shimaoka K 1977 *Phys. Rev.* **B15** 4392

[23] Gesi K 1992 *J. Phys. Soc. Japan* **61** 1225

[24] Shigematsu H, Mashiyama H, Oohara Y and Ohshima K 1996 *Physica* **B219**&**220** 611

[25] Wada M, Sawada A and Ishibashi Y 1981 *J. Phys. Soc. Japan* **50** 531

[26] Nomoto K, Atake T, Chaudhuri B K and Chihara H, *J. Phys. Soc. Japan* **52** 3475

[27] Mashiyama H 1991 *J. Phys. Soc. Japan* **60** 180

[28] Yamamoto A and Ishihara K N 1988 *Acta Crystallogr.* **A44** 707

[29] Perez-Mato J M and Iglesias J E 1977 *Acta Crystallogr.* **A33** 466

Table 1. Crystal data of phases III, IV and V in Rb_2ZnBr_4.

Transition temperature (K)		$T_4 = 76$	$T_3 = 112$
Phase	V	IV	III
Space group	$C1c1$	$P11b$[a]	$P2_1cn$
Polar or antipolar	Ferroelectricity$//a$ Ferroelectricity$//c$	Ferroelectricity$//a$ Antiferroelectricity$//b$	Ferroelectricity$//a$
Extinction rules for systematic absence	$h_s0l_s : l_s = 2n+1$ $h_sk_sl_s : h_s + k_s = 2n+1$	$h_s0l_s : l_s = 2n+1$ $h_sk_sl_s : h_s + k_s = 2n+1$ $h_sk_s0 : h_s + k_s = 4n+2$ and $h_s, k_s = 2n$	$h_s0l_s : l_s = 2n+1$ $h_sk_s0 : h_s + k_s = 2n+1$
Angle (°)	$\alpha = \gamma = 90,\ \beta \neq 90$	$\alpha = \beta = \gamma = 90$	$\alpha = \beta = \gamma = 90$
Cell dimension	$2a_0 \times 2b_0 \times 3c_0$	$2a_0 \times 2b_0 \times 3c_0$	$a_0 \times b_0 \times 3c_0$

[a] under the basis defined by equation (7)

Table 2. Symmetry operations of the models IV_B, IV_C and IV_D.

Model	Symmetry operations	
IV_B	$[1]_A\ x,\ y,\ z$	$[2]_A\ x,\ y+\frac{1}{2},\ \overline{z}+\frac{1}{2}$
	$[3]_B\ y+\frac{3}{4},\ x+\frac{1}{4},\ z+\frac{1}{2}$	$[4]_B\ y+\frac{3}{4},\ x+\frac{3}{4},\ \overline{z}$
IV_C	$[1]_A\ x,\ y,\ z$	$[2]_A\ x,\ y+\frac{1}{2},\ \overline{z}+\frac{1}{2}$
	$[3]_C\ y+\frac{1}{4},\ x+\frac{3}{4},\ z+\frac{1}{2}$	$[4]_C\ y+\frac{1}{4},\ x+\frac{1}{4},\ \overline{z}$
IV_D	$[1]_D\ x,\ y,\ z$	$[2]_D\ x+\frac{1}{2},\ y+\frac{1}{2},\ z$
	$[3]_D\ x,\ \overline{y},\ z+\frac{1}{2}$	$[4]_D\ x+\frac{1}{2},\ \overline{y}+\frac{1}{2},\ z+\frac{1}{2}$
	$[5]_D\ x+\frac{1}{4},\ y+\frac{1}{4},\ \overline{z}+\frac{1}{2}$	$[6]_D\ x+\frac{3}{4},\ y+\frac{3}{4},\ \overline{z}+\frac{1}{2}$
	$[7]_D\ x+\frac{1}{4},\ \overline{y}+\frac{3}{4},\ \overline{z}$	$[8]_D\ x+\frac{3}{4},\ \overline{y}+\frac{1}{4},\ \overline{z}$

Table 3. Relationship between structure factors and indices in phases IV (models $\mathrm{IV_A}$, $\mathrm{IV_B}$, $\mathrm{IV_C}$ and $\mathrm{IV_D}$) and V when the domain ratio deviates from 1 : 1. The Miller indices are referred to the $2a_0 \times 2b_0 \times 3c_0$ cell dimension.

Phase IV	model $\mathrm{IV_A}$	$\lvert F(h_\mathrm{s}k_\mathrm{s}l_\mathrm{s})\rvert = \lvert F(\overline{h_\mathrm{s}}k_\mathrm{s}l_\mathrm{s})\rvert = \lvert F(h_\mathrm{s}k_\mathrm{s}\overline{l_\mathrm{s}})\rvert = \lvert F(\overline{h_\mathrm{s}k_\mathrm{s}l_\mathrm{s}})\rvert,$	
	$P11b$	$\lvert F(h_\mathrm{s}\overline{k_\mathrm{s}}l_\mathrm{s})\rvert = \lvert F(\overline{h_\mathrm{s}}k_\mathrm{s}l_\mathrm{s})\rvert = \lvert F(h_\mathrm{s}\overline{k_\mathrm{s}l_\mathrm{s}})\rvert = \lvert F(\overline{h_\mathrm{s}}k_\mathrm{s}\overline{l_\mathrm{s}})\rvert$	
	models $\mathrm{IV_B}$ and $\mathrm{IV_C}$	$\lvert F(h_\mathrm{s}k_\mathrm{s}l_\mathrm{s})\rvert = \lvert F(\overline{h_\mathrm{s}k_\mathrm{s}}l_\mathrm{s})\rvert = \lvert F(h_\mathrm{s}k_\mathrm{s}\overline{l_\mathrm{s}})\rvert = \lvert F(\overline{h_\mathrm{s}k_\mathrm{s}l_\mathrm{s}})\rvert$	main
	$P11b$ base	$= \lvert F(h_\mathrm{s}\overline{k_\mathrm{s}}l_\mathrm{s})\rvert = \lvert F(\overline{h_\mathrm{s}}k_\mathrm{s}l_\mathrm{s})\rvert = \lvert F(h_\mathrm{s}\overline{k_\mathrm{s}l_\mathrm{s}})\rvert = \lvert F(\overline{h_\mathrm{s}}k_\mathrm{s}\overline{l_\mathrm{s}})\rvert$	reflections
		$\lvert F(h_\mathrm{s}k_\mathrm{s}l_\mathrm{s})\rvert = \lvert F(\overline{h_\mathrm{s}k_\mathrm{s}}l_\mathrm{s})\rvert = \lvert F(h_\mathrm{s}k_\mathrm{s}\overline{l_\mathrm{s}})\rvert = \lvert F(\overline{h_\mathrm{s}k_\mathrm{s}l_\mathrm{s}})\rvert,$	superlattice
		$\lvert F(h_\mathrm{s}\overline{k_\mathrm{s}}l_\mathrm{s})\rvert = \lvert F(\overline{h_\mathrm{s}}k_\mathrm{s}l_\mathrm{s})\rvert = \lvert F(h_\mathrm{s}\overline{k_\mathrm{s}l_\mathrm{s}})\rvert = \lvert F(\overline{h_\mathrm{s}}k_\mathrm{s}\overline{l_\mathrm{s}})\rvert$	reflections
	model $\mathrm{IV_D}$	$\lvert F(h_\mathrm{s}k_\mathrm{s}l_\mathrm{s})\rvert = \lvert F(\overline{h_\mathrm{s}k_\mathrm{s}}l_\mathrm{s})\rvert = \lvert F(h_\mathrm{s}k_\mathrm{s}\overline{l_\mathrm{s}})\rvert = \lvert F(\overline{h_\mathrm{s}k_\mathrm{s}l_\mathrm{s}})\rvert$	main
	$C1c1$ base	$= \lvert F(h_\mathrm{s}\overline{k_\mathrm{s}}l_\mathrm{s})\rvert = \lvert F(\overline{h_\mathrm{s}}k_\mathrm{s}l_\mathrm{s})\rvert = \lvert F(h_\mathrm{s}\overline{k_\mathrm{s}l_\mathrm{s}})\rvert = \lvert F(\overline{h_\mathrm{s}}k_\mathrm{s}\overline{l_\mathrm{s}})\rvert$	reflections
		$\lvert F(h_\mathrm{s}k_\mathrm{s}l_\mathrm{s})\rvert = \lvert F(h_\mathrm{s}\overline{k_\mathrm{s}}l_\mathrm{s})\rvert = \lvert F(\overline{h_\mathrm{s}}k_\mathrm{s}\overline{l_\mathrm{s}})\rvert = \lvert F(\overline{h_\mathrm{s}k_\mathrm{s}l_\mathrm{s}})\rvert,$	superlattice
		$\lvert F(h_\mathrm{s}k_\mathrm{s}\overline{l_\mathrm{s}})\rvert = \lvert F(\overline{h_\mathrm{s}k_\mathrm{s}}l_\mathrm{s})\rvert = \lvert F(\overline{h_\mathrm{s}}k_\mathrm{s}l_\mathrm{s})\rvert = \lvert F(h_\mathrm{s}\overline{k_\mathrm{s}l_\mathrm{s}})\rvert$	reflections
Phase V		$\lvert F(h_\mathrm{s}k_\mathrm{s}l_\mathrm{s})\rvert = \lvert F(h_\mathrm{s}\overline{k_\mathrm{s}}l_\mathrm{s})\rvert = \lvert F(\overline{h_\mathrm{s}}k_\mathrm{s}\overline{l_\mathrm{s}})\rvert = \lvert F(\overline{h_\mathrm{s}k_\mathrm{s}l_\mathrm{s}})\rvert,$	
	$C1c1$	$\lvert F(h_\mathrm{s}k_\mathrm{s}\overline{l_\mathrm{s}})\rvert = \lvert F(\overline{h_\mathrm{s}k_\mathrm{s}}l_\mathrm{s})\rvert = \lvert F(\overline{h_\mathrm{s}}k_\mathrm{s}l_\mathrm{s})\rvert = \lvert F(h_\mathrm{s}\overline{k_\mathrm{s}l_\mathrm{s}})\rvert$	

Figure captions

Figure 1. Phonon dispersion curves in an extended-zone scheme on the (ξ ξ 0) line at 130 K. The solid line for the degenerated TO mode show the result of fitting of for equation (1) to the data. On the other hand, the solid line for the higher TO branch is just a guide to the eye.

Figure 2. Energy scans with constant Q within the optic mode region at 130 K. They correspond to $\xi = 0.575$, 0.60, 0.625, 0.70 and 0.75 in figure 1.

Figure 3. Phonon dispersions curves of the degenerated TO mode in an extended-zone scheme on the (ξ ξ 0) line at 290, 250, 160 and 130 K.

Figure 4. Energy scans with constant Q at $\frac{1}{2}\frac{9}{2}0_{Pmcn}$ below T_4. The excitation peaks of the soft modes A and S are indicated by arrows.

Figure 5. Energy scans with constant Q at $\xi = 0.55$ below T_4. The excitation peaks of the soft modes A and S are indicated by arrows.

Figure 6. Phonon dispersion curves in an extended-zone scheme on the (ξ ξ 0) line at 50 K.

Figure 7. Temperature dependence of the observed mode frequencies at the S point.

Figure 8. The ω-scan profiles of the 400_{Pmcn} reflection with the b-axis as the rotating axis. They were measured at 120 K, and 100 K to 10 K with a 10 K interval.

Figure 9. The temperature dependence of the deviation $\Delta\beta$ of the monoclinic angle from 90° on cooling.

Figure 10. The temperature dependence of the integrated intensity of the 410_{Pmcn} Bragg reflection on heating and on cooling.

Figure 11. Schematic representation of the ($hk0$) reciprocal plane. Large full circles, small full circles and open circles, and open triangles indicate existing positions of the Bragg reflections in phase III, the additional superlattice ones in phase IV and the additional Bragg ones in phase V, respectively. Large full circles and small full circles indicate positions of the reflections for the single domain structure characterized by the reciprocal vectors $A^*_{\rm IV}$, $B^*_{\rm IV}$ and $C^*_{\rm IV}$.

Figure 12. Projection of the structure between $z = 0$ and $\frac{1}{3}$ along the c-axis in phases III, IV and V. $ZnBr_4$ tetrahedra are indicated by triangles and are set at the mean positions of the normal structure. All Rb ions are omitted for simplicity. The primitive unit cells in phases III, IV (models IV_A, IV_B and IV_C) and V are denoted by dotted, dashed and solid lines, respectively. The cell for model IV_D is formed by the same cell as for phase V.

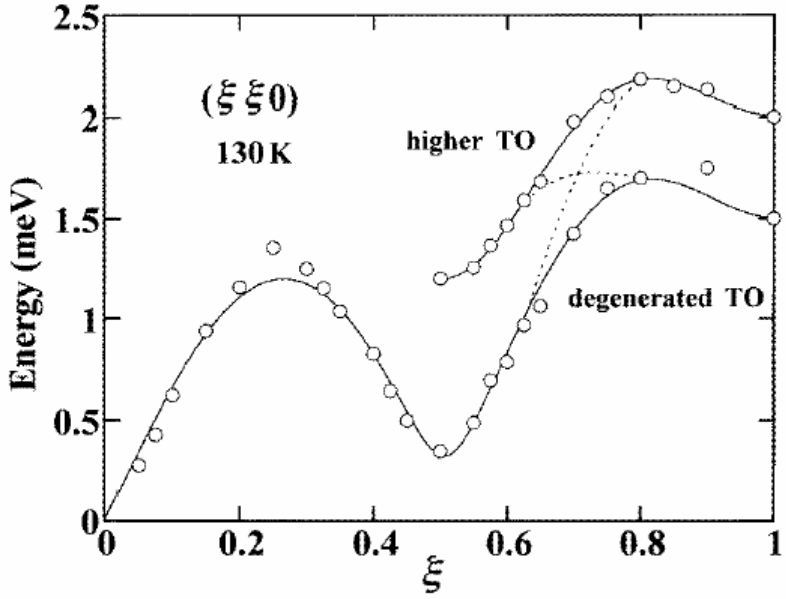
(ξ ξ 0)
130 K
higher TO
degenerated TO
Energy (meV)
ξ
2.5
2
1.5
1
0.5
0
0
0.2
0.4
0.6
0.8
1

Fig. 1.

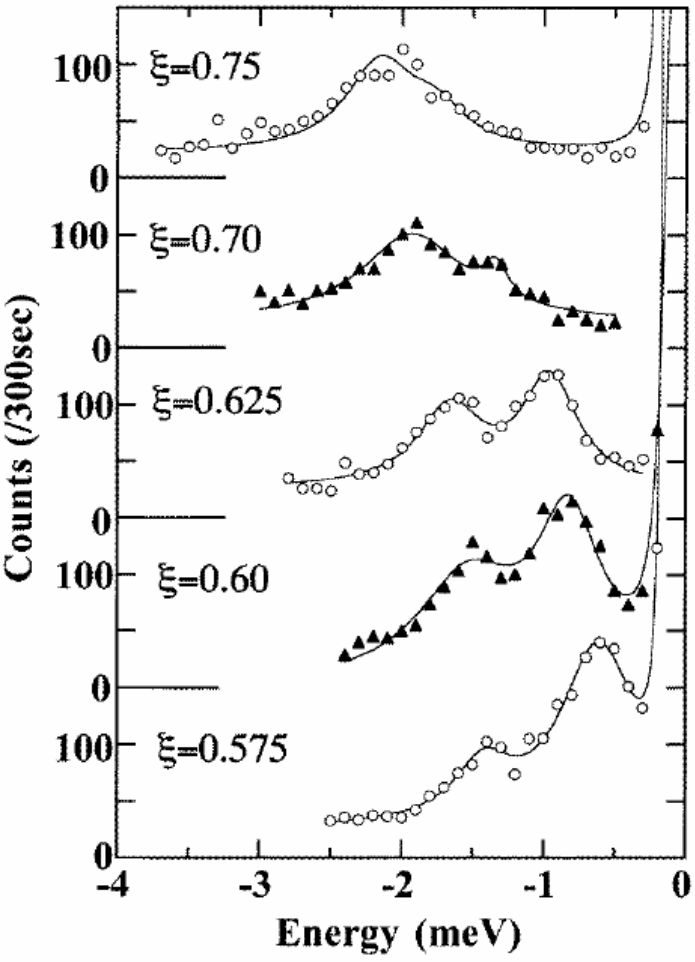
ξ=0.75
ξ=0.70
ξ=0.625
ξ=0.60
ξ=0.575
Counts (/300sec)
Energy (meV)
100
0
-4
-3
-2
-1
0

Fig. 2.

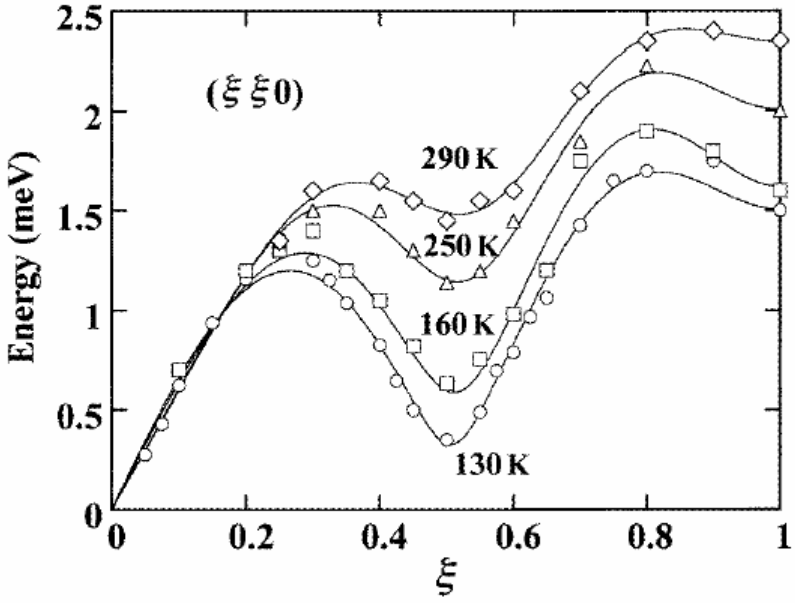
(ξ ξ 0)
290 K
250 K
160 K
130 K
Energy (meV)
ξ
2.5
2
1.5
1
0.5
0
0
0.2
0.4
0.6
0.8
1

Fig. 3.

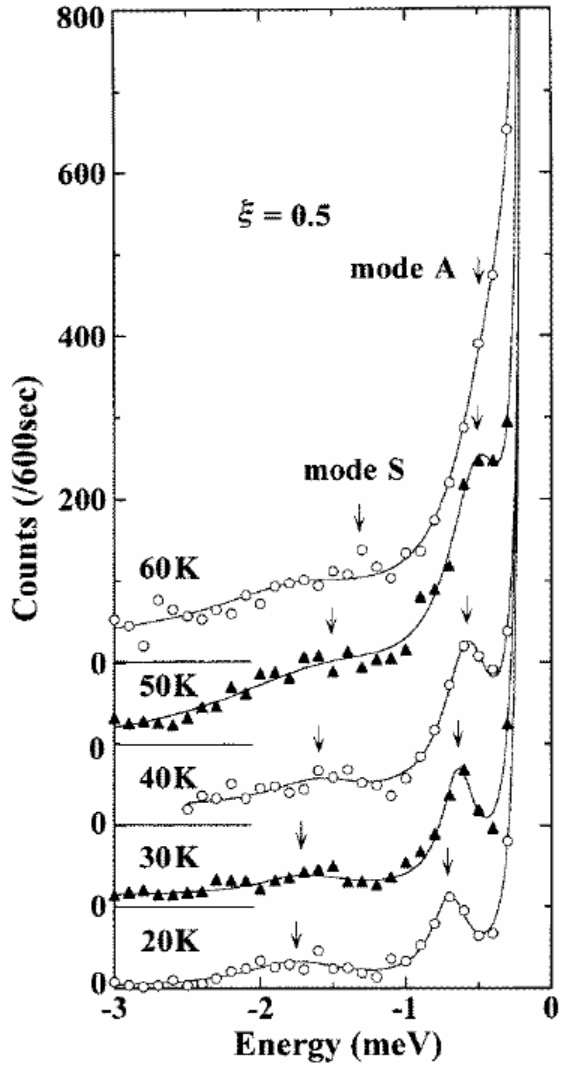
ξ = 0.5
mode A
mode S
60 K
50 K
40 K
30 K
20 K
Counts (/600sec)
Energy (meV)
800
600
400
200
0
-3
-2
-1
0

Fig. 4.

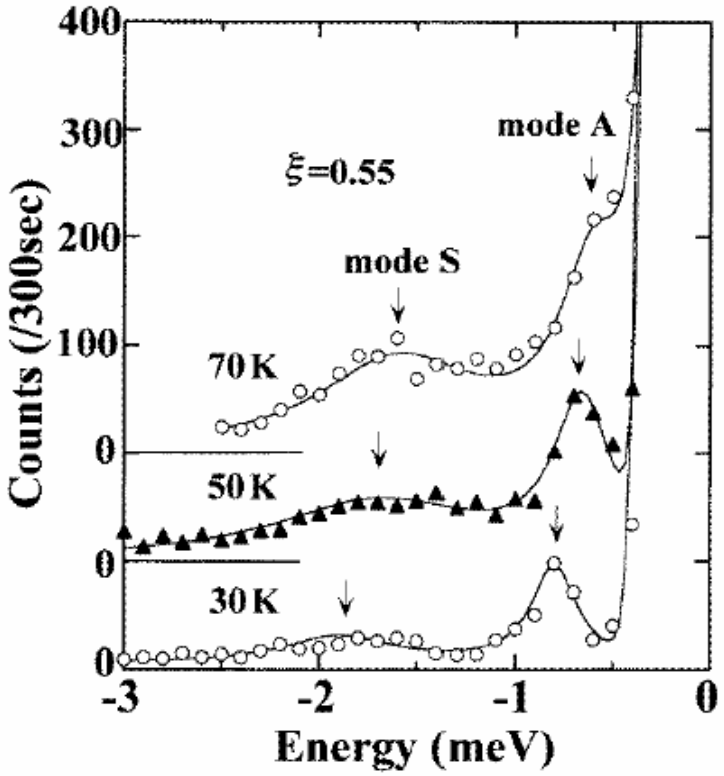
400
300
200
100
0
0
0
Counts (/300sec)
ξ=0.55
mode A
mode S
70 K
50 K
30 K
-3
-2
-1
0
Energy (meV)

Fig. 5.

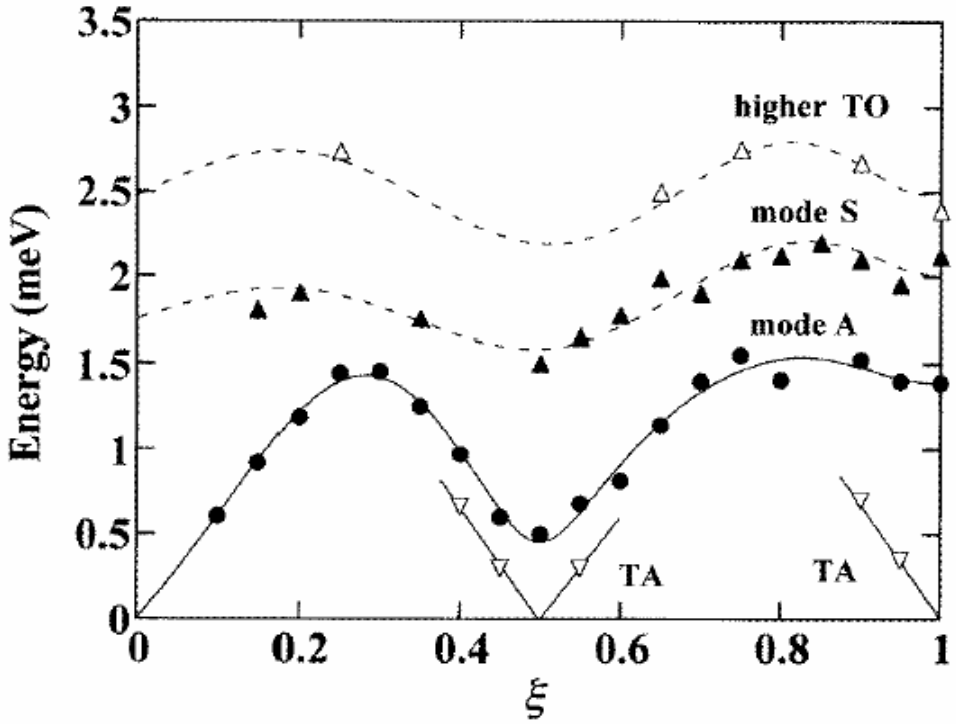
3.5
3
2.5
2
1.5
1
0.5
0
Energy (meV)
higher TO
mode S
mode A
TA
TA
0
0.2
0.4
0.6
0.8
1
ξ

Fig. 6.

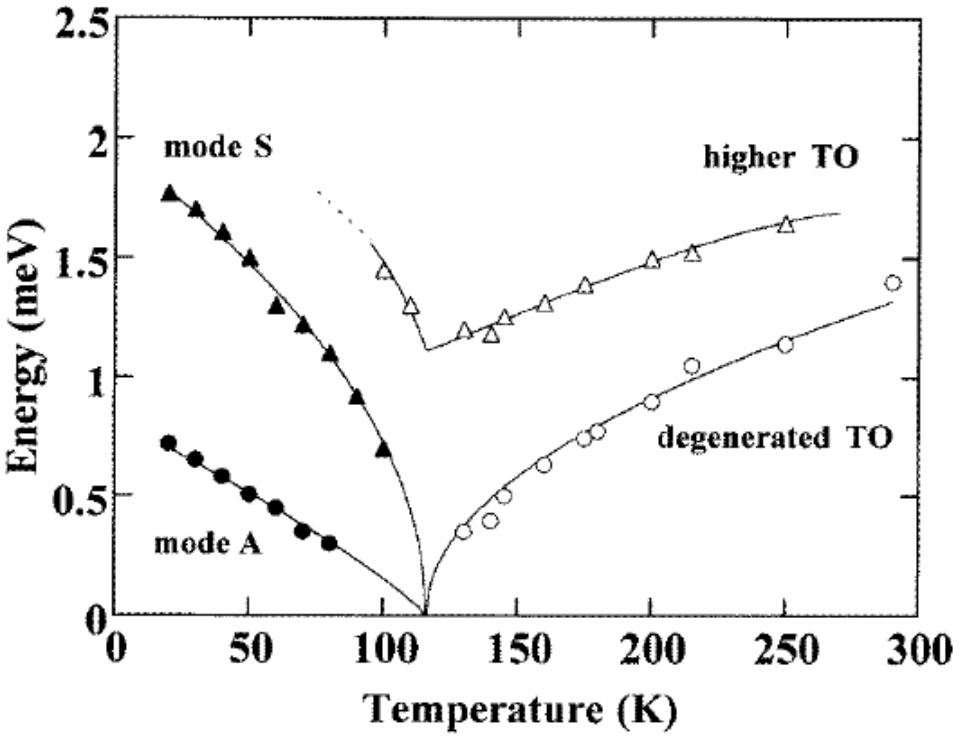
2.5
2
1.5
1
0.5
0
Energy (meV)
mode S
higher TO
degenerated TO
mode A
0
50
100
150
200
250
300
Temperature (K)

Fig. 7.

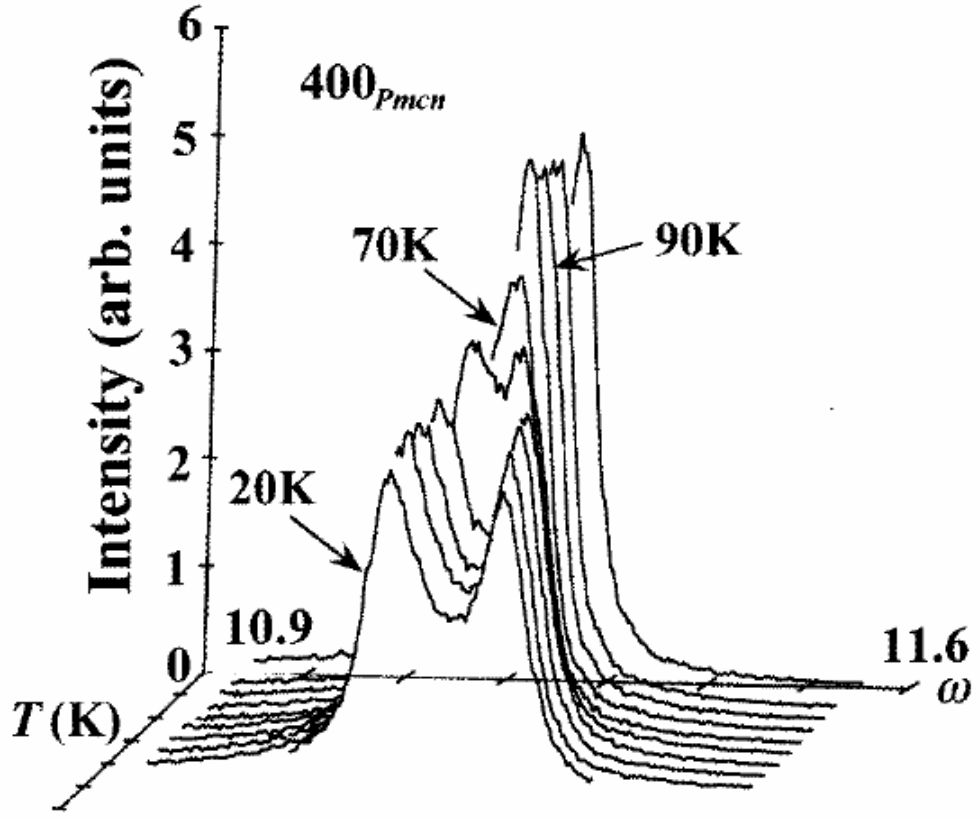
6
5
4
3
2
1
0
Intensity (arb. units)
400Pmcn
70K
90K
20K
10.9
11.6
ω
T (K)

Fig. 8.

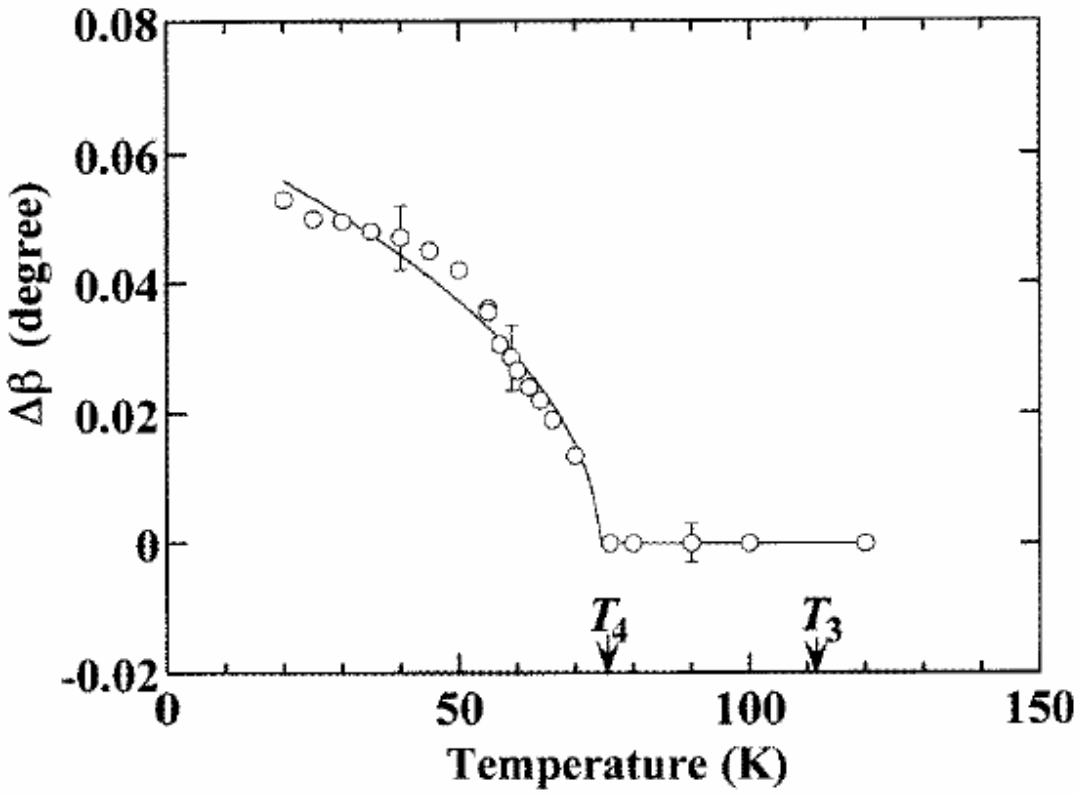
0.08
0.06
0.04
0.02
0
-0.02
Δβ (degree)
T_4
T_3
0
50
100
150
Temperature (K)

Fig. 9.

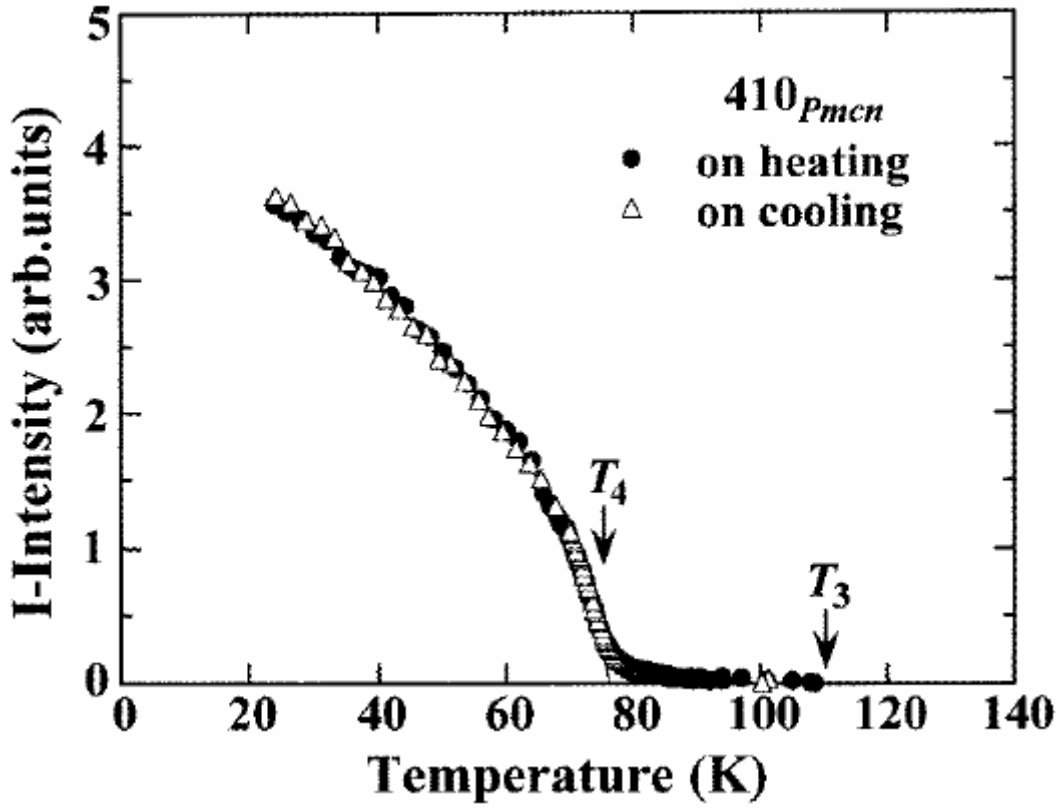
5
4
3
2
1
0
I-Intensity (arb.units)
410_{Pmcn}
on heating
on cooling
T_4
T_3
0
20
40
60
80
100
120
140
Temperature (K)

Fig. 10.

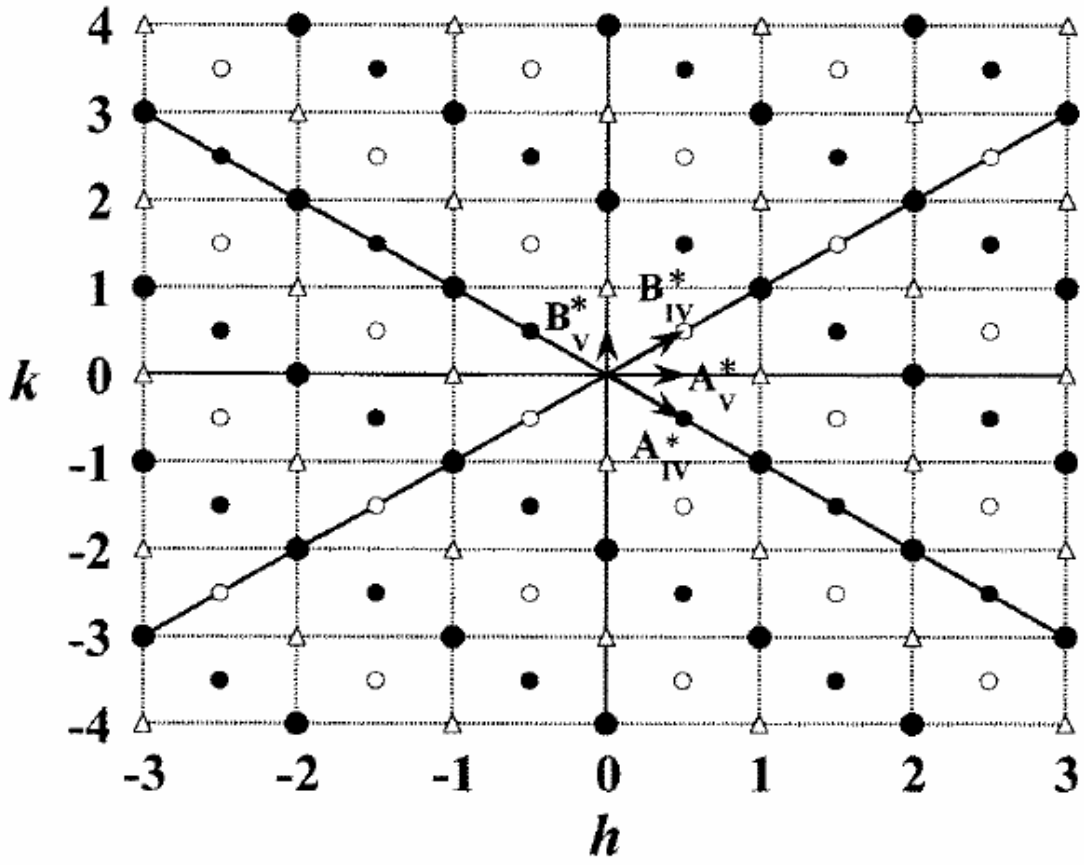

Fig. 11.

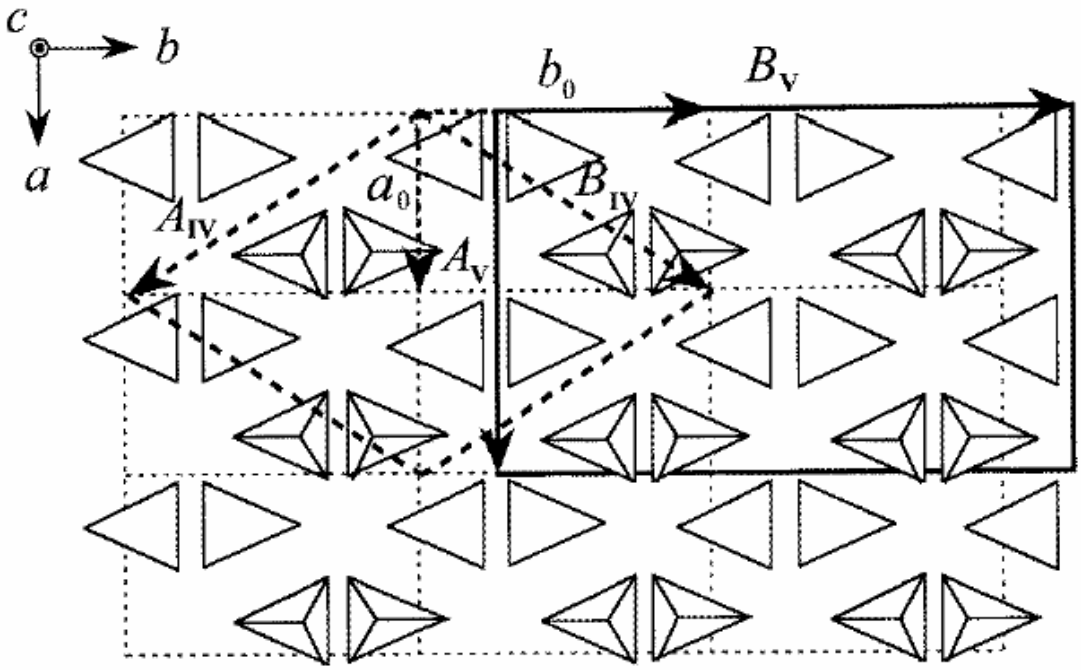

Fig. 12.